



Aerodynamic Instability of Circular Slender Structures Due to Bistable Flow Activity

Adel Benidir Dr Researcher, Olivier Flamand Eng., Grigorios Dimitriadis Prof. Dr & Philippe Delpech Dr Eng.

To cite this article: Adel Benidir Dr Researcher, Olivier Flamand Eng., Grigorios Dimitriadis Prof. Dr & Philippe Delpech Dr Eng. (2022) Aerodynamic Instability of Circular Slender Structures Due to Bistable Flow Activity, Structural Engineering International, 32:1, 71-77, DOI: [10.1080/10168664.2021.1929670](https://doi.org/10.1080/10168664.2021.1929670)

To link to this article: <https://doi.org/10.1080/10168664.2021.1929670>



Published online: 29 Jun 2021.



Submit your article to this journal [↗](#)



Article views: 96




View related articles [↗](#)



View Crossmark data [↗](#)

Aerodynamic Instability of Circular Slender Structures Due to Bistable Flow Activity

Adel Benidir, Dr Researcher, National Center of Integrated Studies and Research on Building Engineering (CNERIB), Souidania, Algiers, Algeria; **Olivier Flamand** , Eng., CSTB, Nantes, France; **Grigorios Dimitriadis**, Prof. Dr, Aerospace and Mechanical Engineering Department, University of Liège, Liège, Belgium; **Philippe Delpech**, Dr Eng., CSTB, Nantes, France.

Contact: abenidir.cnerib@gmail.com

DOI: 10.1080/10168664.2021.1929670

Abstract

Slender structures with circular cylindrical cross-sections are very common in civil engineering, industrial equipment and bridge engineering. Such long cylinders subjected to wind are columns, piles, long cables, chimney, pylons and others. On long cables, an instability called dry galloping has been recently theorized to be linked to an unpredictable jump state occurring once the boundary layers of the circular cylinder changes from laminar to turbulent. With a non-stationary character, the force generated at the critical flow regime is named bi-stable activity. In this work, the birth of bi-stable flow activity around a circular cylinder made of high-density polyethylene is studied experimentally in a wind tunnel. The pressure pattern is linearly decomposed and geometric modes governing the bi-stable activity as a function of circularity defect are created. The results show that the energy of the non-stationary load observed at the critical flow regime depends strongly on the circularity defect. Furthermore, the inclination angle of 60° confers a significant increase in the energy of the bi-stable flow mode when an unsteady asymmetric reattachment event occurs. The paper also highlights the variability of the mean drag coefficient as a function of the macroscopic defect.

Keywords: Bridge cable aerodynamics; dry galloping; critical flow regime; circularity defect; bi-stability

Introduction

Slender structures with an approximately circular cross-section are extensively employed in the civil engineering industry. Elements with a higher height-to-width ratio are classed as slender structures. Such structures are designed and built to resist external forces such as static and dynamic loads.

Inclined long cables in cable-stayed bridges can experience large displacements when the cable covers are subjected to wind load under dry conditions. This phenomenon is called dry galloping (DG). This event has been observed at a specific flow regime^{1,2} and the assumed excitation is exclusively linked to the aerodynamic behavior of the cable.³ Various theories have been advanced to explain the triggering mechanism behind cable vibrations with high amplitudes. Ref. [4] described the mechanism of dry galloping as similar to the one causing vibration when a splitter plate is placed in the wake of a circular cylinder. A second

interpretation of the origin of dry galloping is derived from Den Hartog galloping. The slightly elliptical cross-sectional shape of cable protection covers is considered likely to create a negative lift slope.⁵ Accordingly, analytical models and unified approaches were developed to prevent dry inclined cable galloping.^{6,7} Thirdly, transition in the critical flow regime has been recently theorized to be the most important parameter causing high cable responses.^{3,8} The term transition here is referring to the passage from laminar to turbulent. Previous studies of many scholars discussed the emergence of the critical Reynolds number regime as another possible contributing factor to dry cable galloping.^{6,9} Ref. [10] supports this last theory by concluding that the contribution of the transition within the critical flow regime is one of the principal parameters governing dry galloping.

In the critical flow regime, transition in the boundary layers around a circular cylinder can be classified into the pre-critical regime (TrBL0), the single

bubble regime (TrBL1), and the two-bubble regime (TrBL2).¹¹ The pre-critical regime means that no transition takes place and the pressure pattern around the circular cylinder is symmetric. Thus, the mean lift force is zero. The single-bubble regime implies that transition appears in just one side of the cylinder imposing an asymmetric pressure distribution. The presence of a non-zero mean lift force is observed. Finally, the two-bubble regime denotes that transition occurs on both sides of the cylinder. The mean pressure pattern becomes symmetric again and the mean lift load disappears. The term bubble describes separation in the laminar boundary layer, transition to turbulent and reattachment. It is worth noting that the classification made in Ref. [11] is based on an upright circular cylinder and time-averaged aerodynamic coefficients. However, the mean drag and lift coefficient are not sufficient to describe transitions between two critical regimes as will be argued later.

Ref. [12] confirmed the relationship between recorded large cable vibrations and particular test parameters. Additionally, a specific cable orientation (See for instance Ref. [13] for the definition of the orientation angles) is assumed to be responsible for dry galloping, as confirmed in Ref. [14]. Ref. [15] argued that the triggering mechanism of dry galloping could be linked to the non-stationary character of the aerodynamic loads. Accordingly, the only event that can be deemed non-stationary at the critical regime is the bistable flow activity. It is important to mention that the presence of such loads has been observed before and after the steady TrBL1 state, so that high-amplitude vibrations can also occur before and after the TrBL1 regime, as reported respectively in Refs. [15, 16].

The unsteady aerodynamic forces acting on circular cylinders in the

transitional Reynolds number range can have a non-stationary random character.^{17,18} Ref. [19] showed the appearance of abrupt jumps in aerodynamic loads during transition from TrBL0 to TrBL1. These unpredictable jumps occur at a constant Reynolds number and can be observed in both static and dynamic tests. Benidir et al.⁸ used bifurcation diagrams and proper orthogonal decomposition to analyze these jumps. This analysis showed that the circularity defect of bridge cable covers can have a significant effect on the jump phenomenon. The importance of cross-sectional shape on other aeroelastic phenomena has been extensively studied. For instance, a counter measure to the rain wind-induced vibration (RWIV) is to add a helical fillet on the surface of smooth cable covers.²⁰ Furthermore, pattern-indented surfaces have been used to mitigate both RWIV and DG phenomena. Comparisons of the effects of helical fillets and pattern indentation can be found in.^{21,22} However, pattern indentation and parallel protuberances can sometimes amplify both phenomena.²³ Additionally, Ref. [24] showed that even in the presence of such mitigation measures, a cable can experience vibrations in the critical flow regime.

The present work places emphasis on the influence of cable inclination and circularity defect on the development of jumps in the aerodynamic loads acting on high-density polyethylene (HDPE) cable protection. The investigation consists of testing a genuine cable cover equipped with a large number of pressure taps in an atmospheric wind tunnel. The measured unsteady pressure pattern is analyzed by means of proper orthogonal decomposition (POD) and important conclusions are drawn.

Experiment

The test section of the atmospheric wind tunnel (4 m in width and 2 m in height) of the Scientific and Technical Centre for Building (CSTB) was used for full-scale measurements of the surface pressures on a cable cover. Static upright and inclined HDPE covers with a diameter of 250 mm are subjected to wind, covering a Reynolds number range from the subcritical to the critical flow regimes. The circular tubes are equipped with 288 pressure taps

distributed in nine rings. The length of the instrumented part of the model is 1 m and the separation between rings is not equidistant (Fig. 1). Each ring encompasses 32 pressure taps made of copper with an inner diameter of 0.8 mm. Thus, the separation angle between two successive pressure taps is 11.25°. The information from the surface is transferred via a short vinyl tube to a pressure sensor with a range of 2500 Pa. The sensors are connected in groups of 32 to a compact pressure scanner. The equipment used for the pressure instrumentation (scanners and tubes) is arranged inside the model. The model is composed of two removable end sections connected to the central instrumented portion. The two static end pieces are designed to rigidify the model and to permit the rotation of the central part.

The surface of the cover is naturally smooth and its characteristics are identical to those used in actual bridge cable covers. The average roughness value ranges from Ra = 1.29 to 1.43 µm. The circularity defect (also called macroscopic defect) of the cover is measured using the setup shown in Fig. 2. A laser displacement sensor with a resolution of 60 µm is placed at an appropriate distance from the rotating cover. The reflection of the laser spot from the cover surface when the cover is pivoting describes the distribution of the macroscopic shape of the cable cover. The measurement of the circularity defect is performed close to the location of the measurement rings and after perforating the pressure taps. The measurement operation is carried out on both sides of each ring.

The turbulence intensity of the free stream blowing towards rings 2 to 8 is $I = 1.1\%$ with a standard deviation of 0.21. A turbulence intensity of 1.38% is recorded at ring 9. The influence of

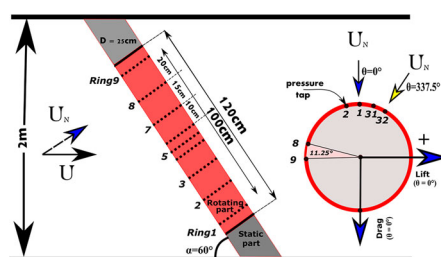


Fig. 1: Wind tunnel arrangement with an inclination angle of $\alpha = 60^\circ$

the flow turbulence on the aerodynamic behavior of the model will not be treated in this paper. However, some interesting and recent conclusions about the contribution of flow turbulence on the aerodynamic behavior of stay cable covers can be found in.²⁵

The upright cable model is subjected to sixteen wind directions. Each wind direction is identified by a rotation angle (θ) corresponding to a specific pressure tap number. The rotation angle is incremented by 22.5° steps. For instance, $\theta = 0^\circ$ and, $\theta = 90^\circ$ denote that pressure taps 1 and 9 respectively lie upstream. The objective of this experiment is to shed light on the influence of the circularity defect on boundary layer transition behavior. The configuration of the cable is limited to one inclination angle, $\alpha = 60^\circ$ (corresponding to an equivalent angle $\Phi = 60^\circ$). At that equivalent angle, high amplitude oscillations of cables with smooth and rough surfaces have been observed.^{9,16,24} One rotation angle ($\theta = 0^\circ$) is tested in this configuration.

Data Analysis

The non-dimensional mean drag and lift coefficients (C_D and C_L) are defined as

$$C_D = \frac{F_D}{(1/2)\rho U^2 S} \quad (1)$$

$$C_L = \frac{F_L}{(1/2)\rho U^2 S} \quad (2)$$

where the drag (F_D) and lift (F_L) forces are calculated by the integration of the pressure distribution around each ring, ρ is the air density, U is the airspeed, $S = DL$ is the reference surface area, D is the diameter and $L = 1$ m is the cover length,

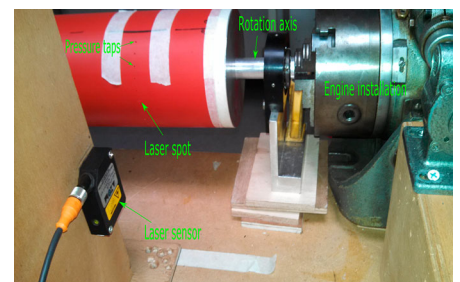


Fig. 2: Setup of the measurement the circularity defect

corresponding to the distance between ring 1 and ring 9.

The analysis of the instantaneous pressure distribution around the cable has been performed using Proper Orthogonal Decomposition (POD). The basic principle of POD is the creation of a mathematical model of an unsteady flow that decouples the spatial from the temporal variations. The technique allows the writing of the surface pressure ($P(x, t)$) in the form.

$$P(x, t) = \sum_{i=1}^N \varphi_i(x) * q_i(t) \quad (3)$$

where $\varphi_i(x)$ are the POD mode shapes depending on the spatial coordinate x . The generalized coordinates $q_i(t)$ represent the time dependence of the pressure. The subscript i refers to the i th mode. It is important to note that the mean pressures are not subtracted from the unsteady pressures. Therefore, the first mode in the present work represents the time-averaged pressure field. The POD process involves the solution of the eigenvalue problem

$$CA = \lambda A \quad (4)$$

where C is the covariance matrix of P , A is the matrix of eigenvectors of C and λ is the diagonal eigen value matrix. More details about POD can be found in.^{26,27}

Results and Discussion

Mean Aerodynamic Coefficients

The variations of the mean drag and lift coefficients with Reynolds number for a rotation angle of $\theta = 22.5^\circ$ are plotted respectively in Fig. 3a, b. The cable is in the upright position (inclination angle $\alpha = 90^\circ$) and all rings are represented in the plot. The identification of the TrBL regime is associated with the drag crisis event. An abrupt decrease in the drag force announces the onset of the critical flow regime. For a circular cylinder, the critical regime is identified directly after the shear layer transition regime where the average C_D is fairly constant. More generally, the critical flow regime is covering the Reynolds number range of $Re = 2 \times 10^5$ to $Re = 5 \times 10^5$.²⁸ By referring to the mean drag coefficient values, the critical Reynolds number is associated with the Reynolds number where C_D falls to 0.8.²⁹ As shown in Fig. 3a, the rings located near the floor and the ceiling of the wind tunnel are not respecting faithfully this condition. It is also important to mention that in the subcritical regime (for instance, $Re = 1.057 \times 10^5$) the values of the mean drag coefficients of the nine rings are dispersed. The difference between the two extreme values is 0.242, which is considered important in comparison to the uncertainty in C_D reported in.²⁹ In addition, the mean and the standard deviation of C_D (Ring 1 to Ring 9) are respectively 1.066 and 0.084. Free stream turbulence and the non-uniform distribution of the

macroscopic defect along the model may cause this dispersion, which is strongly reduced in the critical flow regime.

At the start of the critical flow regime, the mean lift coefficient values increase steadily until they jump to a peak. This peak represents the establishment of the single-bubble regime (steady TrBL1). For higher Reynolds numbers, the progressive decrease of the absolute value of the mean lift coefficient denotes the occurrence of the second transition in the boundary layers, leading to a definite suppression of the mean lift force (steady TrBL2). Figure 3b shows also that the maximum values of the mean lift coefficients are dispersed. For instance, $C_L = -1.21$ is obtained at the location of ring 3 where as ring 7 gives $C_L = -0.725$. The asymmetry created by the single-bubble regime results in the negative sign of the lift coefficient for all the rings. The appearance of a steady TrBL1 regime on one side along the cylinder may be due to the spatial correlation of the circularity defect.⁸ Consequently, a thorough analysis of the influence of the macroscopic defect on the pressure pattern around the cover is mandatory. To this end, and to neutralize the effect of free stream turbulence on the description of the influence of the circularity defect on the aerodynamic behavior of the cable, the mean aerodynamic coefficients of a single ring will be used. Ring 5 located in the mid-span section is chosen.

Figure 4a,b plot respectively the mean drag and lift coefficients obtained at ring 5 for two different wind directions ($\theta = 22.5^\circ$ and $\theta = 67.5^\circ$). The distribution of the macroscopic defect for each wind direction is also indicated. The variation of the drag coefficients with Reynolds numbers demonstrates the establishment of the TrBL1 regime at the same Reynolds number for $\theta = 22.5^\circ$ and $\theta = 67.5^\circ$. However, for higher Reynolds numbers, the aerodynamic behavior of the cover depends on orientation as the second transition regime is progressively installed. The TrBL2 regime occurs at $Re = 3.1 \times 10^5$ for $\theta = 22.5^\circ$ and at $Re = 3.4 \times 10^5$ for $\theta = 67.5^\circ$. The mean lift and drag coefficients at TrBL2 also depend on the cover's orientation. The difference between the drag coefficient at $\theta = 22.5^\circ$ ($C_{D(TrBL2), \theta = 22.5^\circ}$) and the drag coefficient at $\theta = 67.5^\circ$

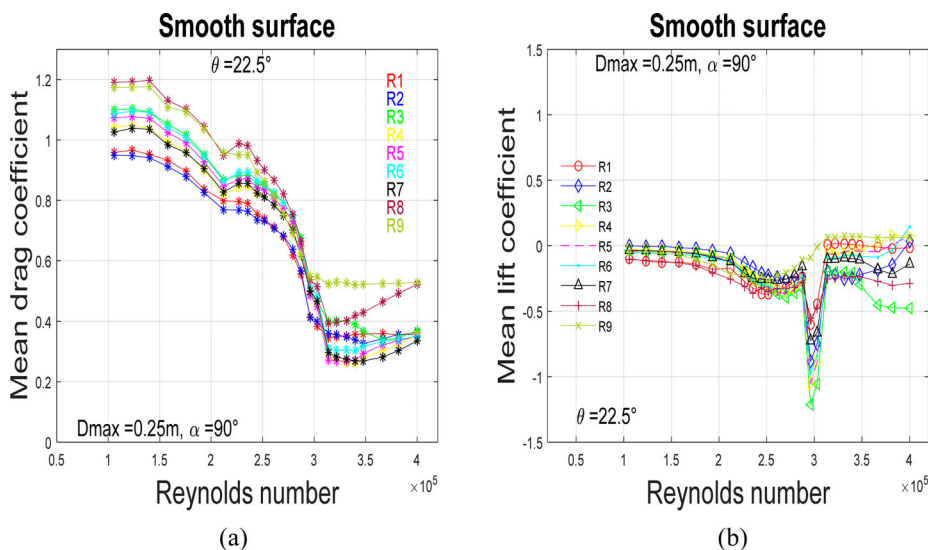


Fig. 3: Mean aerodynamic coefficients, $\alpha = 90^\circ$, $\theta = 22.5^\circ$: (a) Drag (b) Lift

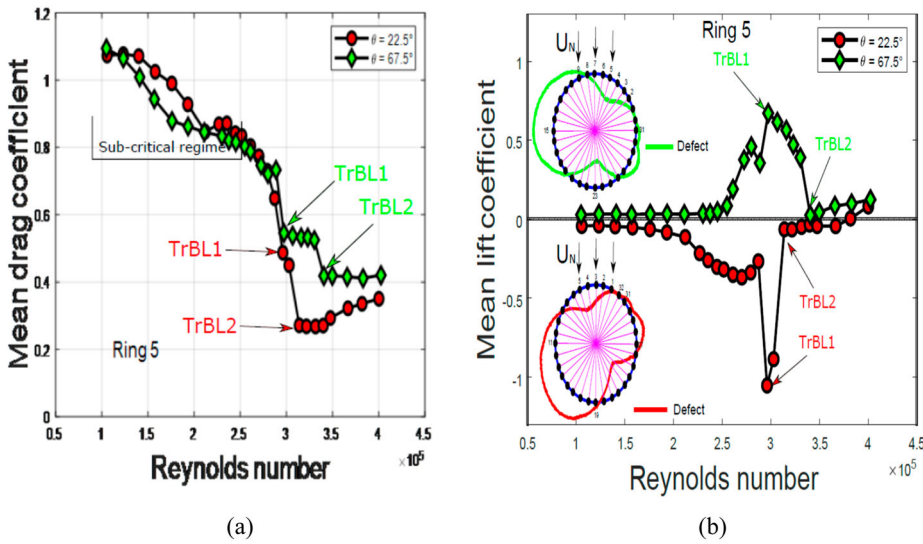


Fig. 4: Mean drag and lift coefficients at ring 5, $\alpha = 90^\circ$, $\theta = 22.5^\circ, 67.5^\circ$: (a) Drag (b) Lift

($C_{D(\text{TrBL2})}$, $\theta = 67.5^\circ$) is 0.146, which is relatively important (53.7% difference). Furthermore, the signs of the mean lift force are opposite in the two orientations.

Even though the incidence of the macroscopic defect on the aerodynamic coefficients (especially the lift) has been demonstrated experimentally,⁸ the results reported in Fig. 4 show that both drag and lift are sensitive to a particular flow regime. A global overview of the influence of the circularity defect on the pressure pattern around the circular cylinder is shown in Fig. 5, which plots the standard deviation of the mean drag (σ_{C_D}) and mean lift (σ_{C_L}) coefficients of ring 5 (for the 16 angles of rotation (N)) as functions of the Reynolds numbers. These standard deviations are

defined as

$$\sigma_{C_D} = \sqrt{\frac{1}{N-1} \sum_{\theta=0^\circ}^{\theta=337.5^\circ} (C_D(\theta) - \overline{C_D})^2};$$

$$\overline{C_D} = \frac{1}{N} \sum_{\theta=0^\circ}^{\theta=337.5^\circ} C_D(\theta);$$

$$N = 16$$

$$\sigma_{C_L} = \sqrt{\frac{1}{N-1} \sum_{\theta=0^\circ}^{\theta=337.5^\circ} (C_L(\theta) - \overline{C_L})^2};$$

$$\overline{C_L} = \frac{1}{N} \sum_{\theta=0^\circ}^{\theta=337.5^\circ} C_L(\theta);$$

$$N = 16$$

for each value of the Reynolds number. The figure shows that the dispersion of the mean aerodynamic coefficients is most important in the critical flow regime. In the sub-critical regime, the mean drag and lift coefficients are significantly less sensitive to the angle of rotation. The large dispersion in the lift coefficient in the critical regime can be explained in part by the asymmetric flow.³⁰ During a complete rotation, the sign of the lift coefficient in the critical flow regime changes,¹⁵ since transition only occurs on one side in the TrBL1 regime. However, the most important observation is the variation of the mean drag coefficient in the critical flow regime which cannot be caused by low test repeatability or free stream turbulence. The

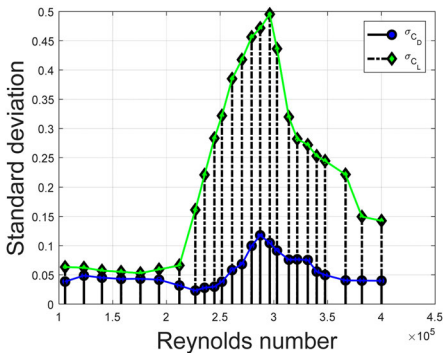


Fig. 5: The standard deviation of the mean drag and lift coefficients for a complete rotation of the cover, $\alpha = 90^\circ$

tests are performed in the same wind tunnel section and the data comes from the same ring (ring 5). Furthermore, the repeatability tests performed in Ref. [25] show an insignificant variability of the force coefficients at a constant Reynolds number. Thus, on a quasi-circular smooth cylinder, the mean drag forces are sensitive to both circularity defect and flow regime. To these authors' knowledge, this conclusion has not been reported elsewhere.

The results presented up to this point concern only mean aerodynamic loads and therefore cannot give any information on the unsteady nature of these loads. For instance, the fact that the mean lift is negative does not mean that the instantaneous lift is also always negative. The unsteady pressure distributions will be presented next in order to demonstrate the occurrence of abrupt jumps in the aerodynamic loads.

POD and Bistable Flow Activity

As mentioned earlier, the TrBL1 state involves asymmetric mean flow, featuring a separation bubble on one side of the cylinder. However, the instantaneous behavior may be such that the separation bubble can abruptly disappear or reappear, either on one side of the cylinder or on both. This phenomenon can lead to unpredictable pressure pattern disturbances¹⁷ and abrupt jumps in the lift coefficient.¹⁹ As there are two possible quasi-stable states (separation bubble between one or the other side), the switching between these two states is named bi-stable activity. The presence and the spatial correlation of bi-stable results. Figure 6 shows the generalized

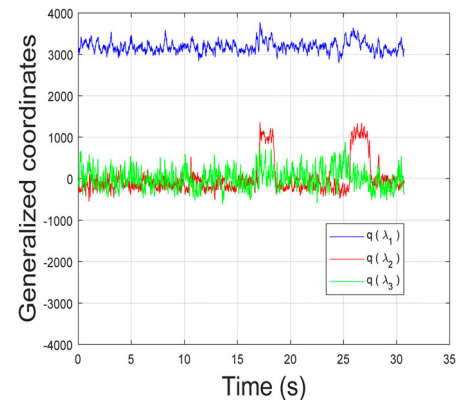


Fig. 6: Three generalized coordinates of the pressure pattern, $\alpha = 90^\circ$, $Re = 2.8 \times 10^5$, $\theta = 67.5^\circ$

coordinates of the first three modes ($q_1(t)$, $q_2(t)$ and $q_3(t)$) for a rotation angle of $\theta=67.5^\circ$, at a Reynolds number of 2.8×10^5 . It is important to note that the unit of the generalized coordinates is Pascal times (weighted) the non-dimensional eigenvalues of A (refer to (4)). In addition, the energy of the modes is represented by the eigenvalues λ_i (see (4)). The values of mean drag and lift coefficients at ring 5 are respectively, $C_{(D, \text{Ring } 5, \theta=67.5^\circ)} = 0.7208$ and $C_{(L, \text{Ring } 5, \theta=67.5^\circ)} = 0.4605$ (see Fig. 4). The generalized coordinate of the first mode is nearly constant throughout the time history, i.e. it represents the mean flow. The generalized coordinate of the second mode undergoes two abrupt jump events at $t = 17$ s and $t = 26$ s. Mode 2 is the most energetic of the unsteady modes and reflects most strongly bistable activity. The generalized coordinate of mode 3 is also nearly constant throughout the time history and its energy is very low, so that it can be neglected in the following discussion.

The mode shapes of modes 1 and 2 are plotted in Fig. 7. Mode 1 shows that the pressure is highest at the stagnation line (labeled θ_{stag} in the following text) and decreases as the flow accelerates in both directions. There is a very low-pressure area centered at the location of $\theta_{\text{stag}} + 90^\circ$ between rings 4 and 9, denoting that the flow is attached there and separates downstream, at approximately $\theta_{\text{stag}} + 110^\circ$. We can conclude that transition has already occurred on these rings and on this side ($>\theta_{\text{stag}}$). On the other side of the cylinder ($<\theta_{\text{stag}}$) there is a low-pressure area only on rings 8 and

9, which implies earlier flow separation on all other rings. As the sign of $q_1(t)$ is always positive, the low-pressure areas never switch sides in time. This mode shape implies that the mean flow has undergone transition on both sides of rings 8–9, only on the left on rings 4–7 and not at all on rings 1–3. This uneven transition state is due to the variation of the cylinder cross-sectional shape. In fact, the ellipticity of the tested model which is defined as the maximum width divided by the minimum width of the cross section varies strongly (see Appendix).

Mode shape 2 in Fig. 7b features a low-pressure area centered around θ_{stag} , reaches 6.09 for the first transition + 90° between rings 1 and 3. The corresponding generalized coordinate is mostly negligible but jumps to significant positive values at two time instances. This means that flow reattaches on the left side of the cylinder between rings 1 and 3 at these time instances, i.e. transition occurs intermittently there. Figures 6 and 7 show that the pressure distribution around the cylinder jumps between two bistable states:

- (1) Transition on side $>\theta_{\text{stag}}$ for rings 4–9 and laminar flow on the opposite side $<\theta_{\text{stag}}$ for all rings except 8 and 9
- (2) Transition on side $>\theta_{\text{stag}}$ for all rings and laminar flow on the opposite side $<\theta_{\text{stag}}$ for all rings except 8 and 9

The important information to add is the frequency of the jump event during a time acquisition. This can be

inferred from the energy of the second mode (magnitude of λ_2), which depends on the number of bistable states, the amplitude and the duration of the jumps (see Appendix B in Ref. [15]). The energy of mode two represents 1.37% of the energy of all the modes. It has been demonstrated that in the critical flow regime, the energy of the second mode increases.⁸ In fact, for the same rotation angle ($\theta=67.5^\circ$) and in the sub-critical regime ($Re=1.76 \times 10^5$), the proportion of the energy of the second mode (λ_2) is 0.48%, i.e. much lower than in the critical regime.

Similarly, the identification of the second unsteady state (TrBL1-TrBL2) could be obtained by the analysis of the generalized coordinates and the mode shapes at a Reynolds number lower than the one identified to be linked to a steady TrBL2. To this end, Figs. 8, 9 show the results of the orthogonal decomposition of the pressure pattern at a Reynolds number of 3.23×10^5 . In this case, the mean flow (mode shape 1 in Fig. 9a) shows that transition has now occurred on all the rings on the side $>\theta_{\text{stag}}$ and rings 6–9 on the other side. Mode 2 denotes additional transition on rings 3–5 on side $<\theta_{\text{stag}}$. The generalized coordinates of the second mode (Fig. 8) indicates the occurrence of very short-duration jumps during the acquisition time (30 s). The proportion of the energy of the second mode (λ_2) attains only 0.23%. Thus, transition from laminar to turbulent occurs during very short time intervals on rings 3–5 on side $<\theta_{\text{stag}}$. Comparing Figs. 7, 9 shows that transition has spread to a larger area of the cylinder

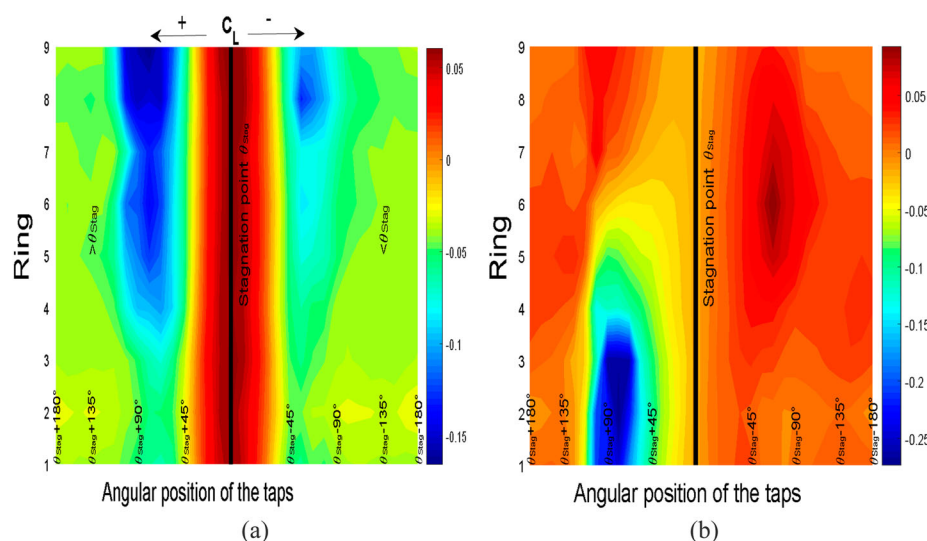


Fig. 7: Mode shapes 1 and 2, $\alpha = 90^\circ$, $Re = 2.8 \times 10^5$, $\theta = 67.5^\circ$: (a) Mode 1 φ_{λ_1} (b) Mode 2 φ_{λ_2}

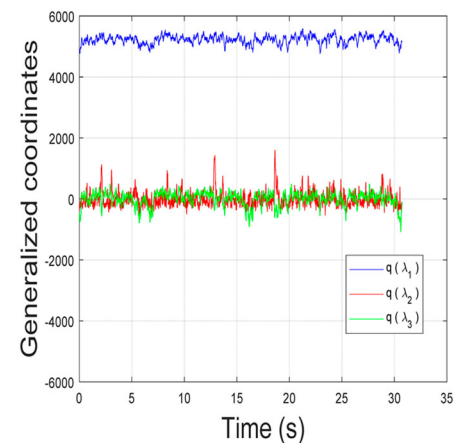


Fig. 8: Three generalized coordinates of the pressure pattern, $\alpha = 90^\circ$, $Re = 3.23 \times 10^5$, $\theta = 67.5^\circ$

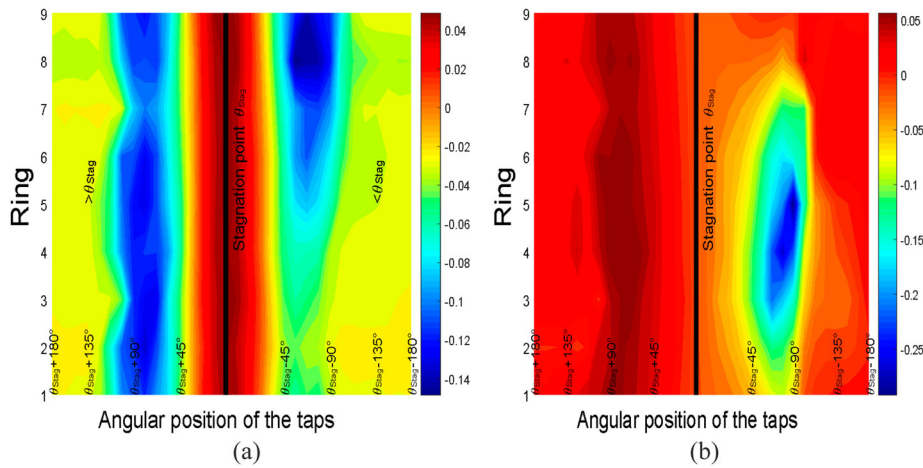


Fig. 9: Mode shapes, $\alpha = 90^\circ$, $Re = 3.23 \times 10^5$, $\theta = 67.5^\circ$: (a) Mode 1 φ_{λ_1} (b) Mode 2 φ_{λ_2}

while comparing Figs. 6, 8 shows that bi-stable activity is less intensive at the higher Reynolds number.

This paragraph has shown that transition is an intermittent phenomenon in the transitional Reynolds number range, leading to at least two stable conditions, one of which is dominant while the other occurs for short periods of time. The frequency and severity of these bistable jumps is represented by the energy of POD mode 2. Furthermore, when the wind comes from direction $\theta = 67.5^\circ$, the bistable activity is more intense in the range TrBL0-TrBL1 than in the range TrBL1-TrBL2. However, to understand the influence of the circularity defect on the occurrence of the bistable activity, a more thorough analysis is presented in the next section.

Bistability and Influence of Circularity Defect and Inclination

The present paragraph investigates the occurrence of bistable activity for the sixteen (16) angles of rotation. Figure 10 the energy of mode 2 as a function of rotation angle. Figure 10a concerns

the range TrBL0-TrBL1 while Fig. 10b concerns the range TrBL1-TrBL2. In the case of the transition from TrBL0 to TrBL1, the distribution of the energy of the bistable activity shows that the orientation of the cable has a significant effect on the bistability of the flow. For instance, at orientation angles of $\theta = 270^\circ$ and $\theta = 315^\circ$, the energy of mode 2 is highest, reaching 2.79% and 2.81% of the total flow energy, respectively. Figure 10b for TrBL1-TrBL2 shows that the strongest bistable activity is obtained at completely different orientation angles. Clearly, the circularity defect has different effects at different Reynolds number ranges. The possibility that a particular form of circularity defect could reduce or suppress bistability at certain orientation angles throughout the transitional Reynolds number range can then be raised.

The effect of an inclination angle of $\alpha = 60^\circ$ on bistable activity has already been analyzed around a smooth circular cylinder with a diameter of 200 mm.¹⁵ However, no distinction was made between the TrBL0-TrBL1

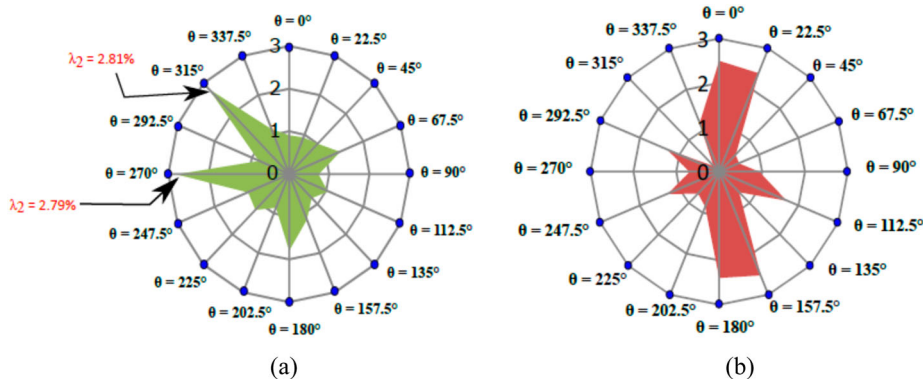


Fig. 10: Distribution of the energy of the mode 2 for a complete rotation: (a) TrBL0-TrBL1 transition (b) TrBL1-TrBL2 transition

and TrBL1-TrBL2 ranges. The effect of inclination angle on the bistable activity was assessed by means of a parameter called the increase factor, i.e. the ratio between the eigenvalue of the second mode (λ_2) at the inclination angle of 60° to the one in the upright configuration ($\alpha = 90^\circ$). At the inclined position, it was found that the energy of the second mode is generally higher than at $\alpha = 90^\circ$. In the present work, one test is performed at $\theta = 0^\circ$ orientation and at inclination angles of $\alpha = 90^\circ$ and $\alpha = 60^\circ$. The results show that the increase factor ($\lambda_2(\alpha = 60^\circ)/\lambda_2(\alpha = 90^\circ)$) reaches 6.09 for the first transition (TrBL0-TrBL1) while its value is only 1.36 in the second transition (TrBL1-TrBL2). Consequently, the authors believe in the strong contribution of the bistable activity in installing dry galloping conditions in the critical inclination angle of 60° , particularly in the TrBL0-TrBL1 range.

Conclusions

In the present manuscript, an experimental investigation around the influence of the circularity defect and the flow regime around a circular cylinder is conducted in the critical Reynolds number range. The experiment consists of measuring the pressure pattern on the surface of a smooth HDPE cable coating with a diameter of 250 mm by mean of 288 pressure taps. Models in an upright and inclined position are subjected to wind load covering the range of the Reynolds number corresponding to the subcritical and the critical regimes. Proper Orthogonal Decomposition is used to analyze the flow unsteadiness. The results are discussed and the main conclusions are the following:

- The mean values of the drag and lift coefficients depend strongly on the circularity defect and on the flow regime around the cylinder.
- The subcritical regime and the critical flow regime have different effects on the aerodynamic coefficients as a complete rotation of the cable around its longitudinal axis is performed.
- In the critical flow regime, the variation of the mean drag coefficient as a function of the circularity defect can be higher than 50%.
- Bistable activity can be more pronounced when the flow transits from the TrBL0 to the TrBL1 regime and

less pronounced when it transits from the TrBL1 to the TrBL2 regime.

- A cable inclination angle of 60° increases significantly the energy of the bistable flow mode, particularly during transition from the TrBL0 to the TrBL1 regime.

ORCID

Olivier Flamand  <http://orcid.org/0000-0002-4885-1117>

References

[1] Larose GL, Zan SJ. The aerodynamic forces on stay cables of cable-stayed bridges in the critical Reynolds number range. In: *Proceedings of the 4th International Symposium on Cable Dynamics*. 2001 May 28–30, Montreal, Canada, 77–84.

[2] Cheng S, Larose GL, Savage MG, Tanaka H. Aerodynamic behaviour of an inclined circular cylinder. *Wind Struct*. 2003; **6**(3): 197–208.

[3] Nikitas N, Macdonald JHG. Aerodynamic forcing characteristics of dry cable galloping at critical Reynolds numbers. *Eur. J. Mech. B Fluid*. 2015; **49**: 243–249.

[4] Matsumoto M, Yagi T, Hatsuda H, Shima T, Tanaka M, Naito H. Dry galloping characteristics and its mechanism of inclined/yawed cables. *J. Wind Eng. Ind. Aerod*. 2010; **98**(6–7): 317–327.

[5] Kumarasena S, Jones NP, Irwin P, Taylor P. Wind-Induced Vibration of Stay Cables. Report No. FHWA-RD-05-083, the Federal Highway Administration. U.S. Department of Transportation. 2007.

[6] Macdonald JHG, Larose G. A unified approach to aerodynamic damping and drag/lift instabilities, and its application to dry inclined cable galloping. *J. Fluids Struct*. 2006; **22**(2): 229–252.

[7] Cheng S, Irwin P, Tanaka H. Experimental study on the wind-induced vibration of a dry inclined cable – part II: proposed mechanisms. *J. Wind Eng. Ind. Aerod*. 2008; **96**(12): 2254–2272.

[8] Benidir A, Flamand O, Gaillet L, Dimitriadis G. Impact of roughness and circularity defect on bridge cables stability. *J. Wind Eng. Ind. Aerod*. 2015; **137**: 1–13.

[9] Cheng S, Larose GL, Savage MG, Tanaka H, Irwin PA. Experimental study on the wind-induced vibration of a dry inclined cable – part I: phenomena. *J. Wind Eng. Ind. Aerod*. 2008; **96**(12): 2231–2253.

[10] Ma W, Liu Q, Matsumoto M. Excitation of the large-amplitude vibrations of a circular cylinder under normal wind conditions in the critical Reynolds number range. *J. Fluids Struct*. 2019; **84**: 318–328.

[11] Zdravkovich MM. *Flow Around Circular Cylinder – Volume 1: Fundamentals*. Oxford: Oxford University Press, 1997.

[12] McTavish S, Raeesi A, D’Auteuil A, Yamauchi K, Sato H. An investigation of the mechanisms causing large-amplitude wind-induced vibrations in stay cables using unsteady surface pressure measurements. *J. Wind Eng. Ind. Aerod*. 2018; **183**: 19–34.

[13] Cosentino N, Flamand O, Ceccoli C. Rain-wind induced vibration of inclined stay cables – part I: experimental investigation and physical explanation. *Wind Struct*. 2003; **6**(6): 471–484.

[14] Vo HD, Katsuchi H, Yamada H, Nishio M. A wind tunnel study on control methods for cable dry-galloping. *J. Front. Struct. Civ. Eng*. 2016; **10**(1): 72–80.

[15] Benidir A, Flamand O, Dimitriadis G. On the aerodynamic characteristics of inclined stay cable sheaths in the critical flow regime. *J. Fluids Struct*. 2020; **99**: 103147.

[16] Jakobsen JB, Andersen TL, Macdonald JHG, Nikitas N, Larose GL, Savage MG, McAuliffe BR. Wind-induced response and excitation characteristics of an inclined cable model in the critical Reynolds number range. *J. Wind Eng. Ind. Aerod*. 2012; **110**: 100–112.

[17] Lin YJ, Miao JJ, Tu JK, Tsai HW. Nonstationary, three-dimensional aspects of Flow Around Circular cylinder at critical Reynolds numbers. *American Institute of Aeronautics and Astronautics Journal*. 2011; **49**(9): 1857–1870.

[18] Cadot O, Desai A, Mittal S, Saxena S, Chandra B. Statistics and dynamics of the boundary layer reattachments during the drag crisis transitions of a circular cylinder. *Phys. Fluids*. 2015; **27**: 014101–1.

[19] Nikitas N, Macdonald JHG, Jakobsen JB, Andersen TL. Critical Reynolds number and galloping instabilities: experiments on circular cylinders. *Exp. Fluid*. 2012; **52**(5): 1295–1306.

[20] Flamand O. Rain wind induced vibration of cables. *J. Wind Eng. Ind. Aerod*. 1995; **57**(2–3): 353–362.

[21] Kleissl K, Georgakis CT. Comparison of the aerodynamics of bridge cables with helical fillets and a pattern-indented surface. *J. Wind Eng. Ind. Aerod*. 2012; **104–106**: 166–175.

[22] Katsuchi H, Yamada H, Sakaki I, Okado E. Wind-Tunnel investigation of the aerodynamic performance of surface-modification cables. *Engineering*. 2017; **3**(6): 817–822.

[23] Hung VD, Katsuchi H, Sakaki I, Ookado E, Arijji R, Yamada H. Aerodynamic performance of spiral-protuberance cable under rain and dry conditions. *J. Struct Eng*. 2016; **62A**: 431–441.

[24] Christiansen H, Jakobsen JB, Macdonald JHG, Larose GL, Bosch HR. Aerodynamics of a stay cable with helical fillets – part I: stability and load characteristics. *J. Wind Eng. Ind. Aerod*. 2018; **177**(June): 376–391.

[25] McTavish S, D’Auteuil A, Raeesi A. Effect of cable surface characteristics and flow turbulence on the aerodynamic behaviour of stay cables in dry conditions. *J. Wind Eng. Ind. Aerod*. 2020. doi:10.1016/j.jweia.2020.104414

[26] Dowell EH, Hall KC, Romanowski MC. Eigen mode analysis in unsteady aerodynamics: reduced order models. *Appl. Mech. Rev*. 1998; **50**(6): 371–385.

[27] Andrianne T, Abdul Razak N, Dimitriadis G. Flow visualization and proper orthogonal decomposition of aeroelastic phenomena. In: Okamoto, Satory (Ed.), *Wind Tunnels*. InTech. ISBN 978-953-307-295-1. 2011.

[28] Achenbach E. Distribution of local pressure and skin friction around a circular cylinder in cross-flow up to $Re=5(10^6)$. *Journal of Fluid Mech*. 1968; **34**(part 4): 625–639.

[29] ESDU 80025. Mean forces, pressures and flow field velocities for circular cylindrical structures: single cylinder with two-dimensional flow.

[30] Schewe G. On the force fluctuations acting on a circular cylinder in cross flow from subcritical up to trans-critical Reynolds numbers. *J. Fluid Mech. Cambridge University Press*. 1983; **133**: 265–285.

Appendix

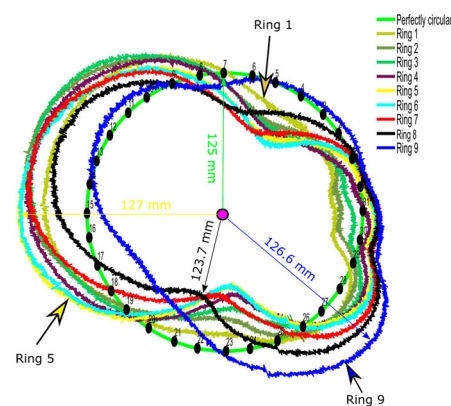


Figure A1: Measured true cross-sectional shape at the locations of all rings.



IABSE SYMPOSIUM GUIMARÃES 2019 (ePDF)

Towards a Resilient Built Environment Risk and Asset Management

www.iabse.org/onlineshop